Article

Spinodal Decomposition and Nucleation and Growth as a Means to Bulk Nanostructured Thermoelectrics: Enhanced Performance in PbSnTe–PbS

John Androulakis, Chia-Her Lin, Hun-Jin Kong, Ctirad Uher, Chun-I Wu, Timothy Hogan, Bruce A. Cook, Thierry Caillat, Konstantinos M. Paraskevopoulos, and Mercouri G. Kanatzidis

J. Am. Chem. Soc., **2007**, 129 (31), 9780-9788• DOI: 10.1021/ja071875h • Publication Date (Web): 13 July 2007

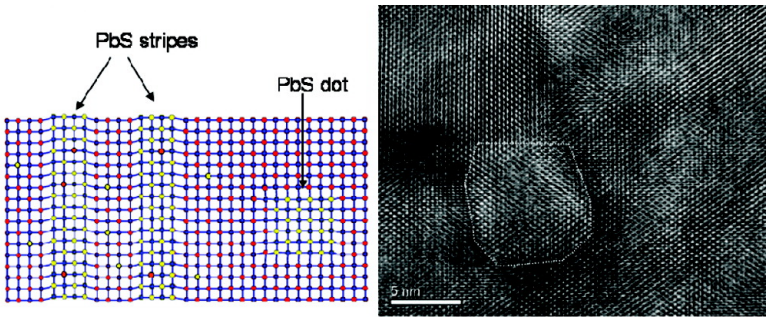

More About This Article

Additional resources and features associated with this article are available within the HTML version:

- Supporting Information
- Links to the 5 articles that cite this article, as of the time of this article download
- Access to high resolution figures
- Links to articles and content related to this article
- Copyright permission to reproduce figures and/or text from this article

View the Full Text HTML

J|A|C|S
ARTICLES
Published on Web 07/13/2007

Spinodal Decomposition and Nucleation and Growth as a Means to Bulk Nanostructured Thermoelectrics: Enhanced Performance in $Pb_{1-x}Sn_xTe-PbS$

John Androulakis,[†] Chia-Her Lin,[†] Hun-Jin Kong,[‡] Ctirad Uher,[‡] Chun-I Wu,[§] Timothy Hogan,[§] Bruce A. Cook,[⊥] Thierry Caillat,[#] Konstantinos M. Paraskevopoulos,[£] and Mercouri G. Kanatzidis*[,†,¶]

Contribution from the Department of Chemistry, Michigan State University, East Lansing, Michigan 48824, Department of Physics, University of Michigan, Ann Arbor, Michigan 48109, Electrical and Computer Engineering and Materials Science and Mechanics, Michigan State University, East Lansing, Michigan 48824, Materials and Engineering Physics Program, 221 Metals Development, Ames Laboratory—Iowa State University, Jet Propulsion Laboratory/California Institute of Technology, 4800 Oak Grove Drive, Pasadena, California, Physics Department, Aristotle University of Thessaloniki, 54124 Greece, and Department of Chemistry, Northwestern University, Evanston, Illinois 60208

Received March 28, 2007; E-mail: m-kanatzidis@northwestern.edu

Abstract: The solid-state transformation phenomena of spinodal decomposition and nucleation and growth are presented as tools to create nanostructured thermoelectric materials with very low thermal conductivity and greatly enhanced figure of merit. The systems $(PbTe)_{1-x}(PbS)_x$ and $(Pb_{0.95}Sn_{0.05}Te)_{1-x}(PbS)_x$ are not solid solutions but phase separate into PbTe-rich and PbS-rich regions to produce coherent nanoscale heterogeneities that severely depress the lattice thermal conductivity. For $x > \sim 0.03$ the materials are ordered on three submicrometer length scales. Transmission electron microscopy reveals both spinodal decomposition and nucleation and growth phenomena the relative magnitude of which varies with *x*. We show that the $(Pb_{0.95}Sn_{0.05}Te)_{1-x}(PbS)_x$ system, despite its nanostructured nature, maintains a high electron mobility (>100 cm^2/V·s at 700 K). At $x \sim 0.08$ the material achieves a very low room-temperature lattice thermal conductivity of ~ 0.4 W/m·K. This value is only 28% of the PbTe lattice thermal conductivity at room temperature. The inhibition of heat flow in this system is caused by nanostructure-induced acoustic impedance mismatch between the PbTe-rich and PbS-rich regions. As a result the thermoelectric properties of $(Pb_{0.95}Sn_{0.05}Te)_{1-x}(PbS)_x$ at $x = 0.04$, 0.08, and 0.16 were found to be superior to those of PbTe by almost a factor of 2. The relative importance of the two observed modes of nanostructuring, spinodal decomposition and nucleation and growth, in suppressing the thermal conductivity was assessed in this work, and we can conclude that the latter mode seems more effective in doing so. The promise of such a system for high efficiency is highlighted by a ZT $\sim$ 1.50 at 642 K for $x \sim 0.08$.

Introduction

Recently, the global need for efficient energy management has renewed interest in solid-state power generation from heat sources with the use of thermoelectric materials. A good thermoelectric material should possess a set of physical properties which have been known ever since the pioneering work of Altenkirch[1,2] who first showed the necessity for a large Seebeck coefficient (S), high electrical conductivity (σ), and low thermal conductivity (κ). These properties define the dimensionless thermoelectric figure of merit, $ZT = S^2\sigma T/\kappa$, where T is the temperature. Nevertheless, the interdependence of the physical parameters defining ZT complicates efforts in developing straightforward strategies for materials with average $ZT > 2$ that could revolutionize the field of energy conversion.

Many efforts to increase ZT have concentrated on reducing κ, which is the sum of the lattice, κ_{lat}, and the electronic, κ_{el}, contributions. Each quantifies the heat-carrying efficiency of phonons for a given lattice and of the charge carriers, respectively. Therefore, choosing the appropriate carrier doping and lattice structure can have a significant impact in optimizing the ZT values. Approaches to reduce the lattice thermal conductivity usually involve phonon scattering by impurity modes or alloying (i.e., making solid solutions). However, alloying causes the adverse effect of charge carrier scattering, and hence electrical resistivity increases, which counteracts the beneficial κ reduction.[3]

[†] Department of Chemistry, Michigan State University.
[‡] University of Michigan.
[§] Electrical and Computer Engineering and Materials Science and Mechanics, Michigan State University.
[⊥] Ames Laboratory—Iowa State University.
[#] Jet Propulsion Laboratory/California Institute of Technology.
[£] Aristotle University of Thessaloniki.
[¶] Northwestern University.
(1) Altenkirch, E. *Phys. Z.* **1909**, *10*, 560−580.
(2) Altenkirch, E. *Phys. Z.* **1911**, *12*, 920−524.

10.1021/ja071875h CCC: $37.00

On the other hand, many theoretical and experimental studies have pointed toward the importance of low-dimensional nanostructured materials[4−7] and other mixed-phase nanocomposites[8−11] as a possible alternative to conventional bulk materials. The physical bases of such studies have been: (i) the quantum confinement effect of charge carriers inside structures with physical dimensions comparable to the electronic wavelength that can potentially increase S, (ii) large expected thermal conductivity reduction stemming from boundary and interface phonon scattering, and (iii) the acoustic phonon spectrum modification of the nanostructures (ultrathin films, nanowires, etc.) which can potentially lead to a further decrease of κ.[12,13] Although, the expected increase in the power factor has not yet been demonstrated,[14,15] all studies seem to be in agreement that a great reduction in thermal conductivity could be achieved through nanostructuring.[11,16−20] Increased thermoelectric efficiency of nanostructures has been reported in a number of thin film multilayers,[4] and the influence of the nanosized regions is also implicated in several bulk nanocomposite systems such as $AgPb_mSbTe_{m+2}$,[21,22] $NaPb_mSbTe_{2+m}$,[23] $Ag_x(Pb,Sn)_mSb_yTe_{2+m}$,[24] and $Pb_{9.6}Sb_{0.2}Te_{10-x}Se_x$.[25]

In this paper we explored the phenomena of spinodal decomposition and nucleation and growth in solids as tools to produce nanostructured thermoelectric materials with very low thermal conductivity. We describe the thermoelectric properties of the PbTe−PbS system which, according to its phase diagram, decomposes spinodally into a naturally nanostructured lattice with compositional fluctuations of a characteristic wavelength of ∼2−5 nm.[26−28] Despite these early reports this system is generally regarded as a normal solid solution. We investigated several PbTe−PbS compositions selected to access different regions of the phase diagram and to probe the nanoscale structure using high-resolution transmission electron microscopy.

We show that this system can achieve a very low $\kappa_{lat} \sim 0.4$ W/m·K at room temperature which is directly comparable to that of artificial thin film superlattice structures[4] where a lattice thermal conductivity of ∼0.33 W/m·K was reported. Furthermore, the system retains a high electron mobility even at high temperatures (>100 $cm^2/V\cdot s$ at 700 K, n-doped). This suggests rather weak scattering of charge carriers at the interfaces of the embedded nanostructures and simultaneously high phonon scattering possibly through the nanostructure-induced acoustic impedance mismatch at interfaces. The highest ZT value observed in these materials so far is 1.50 at 642 K for the composition of 8% PbS in PbTe.

Experimental Section

Synthesis. Samples of $(PbTe)_{1-x}(PbS)_x$ ($x = 0.04$, 0.08, 0.16, and 0.30) were prepared after mixing appropriate ratios of high-purity elemental starting materials and 0.055 mol % of PbI_2 as an n-type dopant. The initial load was sealed in an aqua regia-cleaned fused-silica tube under vacuum and heated at 1273 K for 6 h. The samples were then rapidly cooled to 773 K and held there for 72 h. In practice, this procedure produces ingots which contain a large density of spherical gas pockets and tends to complicate the full characterization of the samples. We have found that a small amount of Sn substitution (∼5%) for Pb cures the effect and produces samples with better structural integrity. For this reason, in most of our studies we focused on these Sn-containing samples. The existence of a biphasic PbTe−PbS system was readily confirmed by powder X-ray diffraction.

Physical Characterization. Quantitative microprobe analyses of the compounds were performed with a JEOL JSM-35C scanning electron microscope equipped with a Tracor Northern EDS detector. Data were acquired using an accelerating voltage of 20 kV and a 40 s accumulation time. The results confirmed the total average sulfur concentrations.

High-Resolution Transmission Electron Microscopy. The nanostructure of $(PbTe)_{1-x}(PbS)_x$ and $(Pb_{0.95}Sn_{0.05}Te)_{1-x}(PbS)_x$ samples was examined using high-resolution transmission electron microscopy (HRTEM). Specimens used for the investigation were prepared as follows. Small square-shape pieces with approximate sizes of 5 mm × 5 mm × 2 mm were first cut from the ingot using a 50 μm tungsten wire on a wire saw (South Bay Technology Inc.). The samples were then hand-polished with subsequently increasing grit (1000−1500) sand paper to about 200−300 μm in thickness. Circular-shape specimens 3 mm in diameter suitable for use in the TEM sample holder were cut using a Gatan model 601 ultrasonic disc cutter. Samples were then thinned using a Gatan model 656 precession dimple grinder and low-angle ion milled (2−4°) to electron transparency using a Gatan model 691 precession ion-polishing system (PIPS). High-resolution transmission electron microscopy images of several pieces cut from different locations of the ingots were recorded at 200 kV using a JEOL JEM 2200FS (field emission TEM).

Thermal Conductivity. The thermal conductivity (κ) was determined as a function of temperature from room temperature to 800 K using the flash diffusivity method (FlashLine 5000, Anter Corp.) at the University of Michigan. The front face of a small disc-shaped sample (Ø = 8 mm; thickness ∼1−2 mm) is irradiated by a short laser burst, and the resulting rear face temperature rise is recorded and

(3) Wood, C. *Rep. Prog. Phys.* **1988**, *51* (4), 459−539.
(4) Harman, T. C.; Taylor, P. J.; Walsh, M. P.; LaForge, B. E. *Science* **2002**, *297* (5590), 2229−2232.
(5) Harman, T. C.; Walsh, M. P.; Laforge, B. E.; Turner, G. W. *J. Electron. Mater.* **2005**, *34* (5), L19−L22.
(6) Li, D. Y.; Huxtable, S. T.; Abramson, A. R.; Majumdar, A. *J. Heat Transfer* **2005**, *127* (1), 108−114.
(7) Venkatasubramanian, R.; Siivola, E.; Colpitts, T.; O'Quinn, B. *Nature* **2001**, *413* (6856), 597−602.
(8) Caylor, J. C.; Coonley, K.; Stuart, J.; Colpitts, T.; Venkatasubramanian, R. *Appl. Phys. Lett.* **2005**, *87* (2), 023105.
(9) Hicks, L. D.; Dresselhaus, M. S. *Phys. Rev. B* **1993**, *47* (24), 16631−16634.
(10) Hicks, L. D.; Dresselhaus, M. S. *Phys. Rev. B* **1993**, *47* (19), 12727−12731.
(11) Kim, W.; Singer, S. L.; Majumdar, A.; Vashaee, D.; Bian, Z.; Shakouri, A.; Zeng, G.; Bowers, J. E.; Zide, J. M. O.; Gossard, A. C. *Appl. Phys. Lett.* **2006**, *88* (24).
(12) Balandin, A. A.; Lazarenkova, O. L., *Appl. Phys. Lett.* **2003**, *82* (3), 415−417.
(13) Zou, J.; Kotchetkov, D.; Balandin, A. A.; Florescu, D. I.; Pollak, F. H. *J. Appl. Phys.* **2002**, *92* (5), 2534−2539.
(14) Broido, D. A.; Reinecke, T. L. *Appl. Phys. Lett.* **1997**, *70* (21), 2834−2836.
(15) Khitun, A.; Wang, K. L.; Chen, G. *Nanotechnology* **2000**, *11* (4), 327−331.
(16) Sootsman, J. R.; Pcionek, R. J.; Kong, H. J.; Uher, C.; Kanatzidis, M. G. *Chem. Mater.* **2006**, *18* (21), 4993−4995.
(17) Androulakis, J.; Pcionek, R.; Quarez, E.; Do, J. H.; Kong, H. J.; Palchik, O.; Uher, C.; D'Angelo, J. J.; Short, J.; Hogan, T.; Kanatzidis, M. G. *Chem. Mater.* **2006**, *18* (20), 4719−4721.
(18) Kim, W.; Zide, J.; Gossard, A.; Klenov, D.; Stemmer, S.; Shakouri, A.; Majumdar, A. *Phys. Rev. Lett.* **2006**, *96* (4), 045901.
(19) Chen, G. *IEEE Trans. Compon. Packag. Technol.* **2006**, *29* (2), 238−246.
(20) Rao, A. M.; Ji, X. H.; Tritt, T. M. *MRS Bull.* **2006**, *31* (3), 218−223.
(21) Hsu, K. F.; Loo, S.; Guo, F.; Chen, W.; Dyck, J. S.; Uher, C.; Hogan, T.; Polychroniadis, E. K.; Kanatzidis, M. G. *Science* **2004**, *303* (5659), 818−821.
(22) Quarez, E.; Hsu, K. F.; Pcionek, R.; Frangis, N.; Polychroniadis, E. K.; Kanatzidis, M. G. *J. Am. Chem. Soc.* **2005**, *127* (25), 9177−9190.
(23) Poudeu, P. F. P.; D'Angelo, J.; Downey, A. D.; Short, J. L.; Hogan, T. P.; Kanatzidis, M. G. *Angew. Chem., Int. Ed.* **2006**, *45* (23), 3835−3839.
(24) Androulakis, J.; Hsu, K. F.; Pcionek, R.; Kong, H.; Uher, C.; Dangelo, J. J.; Downey, A.; Hogan, T.; Kanatzidis, M. G. *Adv. Mater.* **2006**, *18* (9), 1170.
(25) Poudeu, P. F. P.; D'Angelo, J.; Kong, H. J.; Downey, A.; Short, J. L.; Pcionek, R.; Hogan, T. P.; Uher, C.; Kanatzidis, M. G. *J. Am. Chem. Soc.* **2006**, *128* (44), 14347−14355.
(26) Darrow, M. S.; White, W. B.; Roy, R. *Trans. Metall. Soc. AIME* **1966**, *236* (5), 654 ff.
(27) Darrow, M. S.; White, W. B.; Roy, R. *Mater. Sci. Eng.* **1969**, *3* (5), 289 ff.
(28) Leute, V.; Volkmer, N. *Z. Phys. Chem. Neue Folge* **1985**, *144*, 145−155.

analyzed. Thermal conductivity (κ) values were calculated using the equation $\kappa = \alpha C_p d$, where α is the thermal diffusivity, C_p is the specific heat (measured using differential scanning calorimetry), and d is the bulk density of the sample (calculated from the sample's geometry and mass). The specific heat was determined in the range $300 \leq T \leq 800$ K at MSU with a Shimadzu DSC-50 differential scanning calorimeter in reference to the specific heat of a sapphire standard sample using Al sample containers. The heat capacities of the sample containers were also measured and carefully extracted. X-ray spectroscopic analysis of the samples at the conclusion of the experiments did not show Al contamination. The thermal diffusivity and heat capacity of samples were also confirmed independently at the Thermophysical Properties Research Laboratory.[29]

Lattice thermal conductivities were obtained by subtracting the carrier contribution from the total thermal conductivity using the equation $\kappa_{(\text{lattice})} = \kappa_{(\text{total})} - \kappa_{(\text{carrier})}$. Here, $\kappa_{(\text{carrier})}$ is expressed by the Wiedemann–Franz Law $\kappa_{(\text{carrier})} = L\sigma T$, where L is the Lorenz number.

Electrical and Optical Properties. Details regarding the experimental apparatus used to determine the charge-transport properties can be found elsewhere.[13,30,31] The results reported in this study have been repeatedly observed on different batches. Unpolarized reflectivity spectra were received at room temperature with a Bruker 113v FTIR spectrophotometer working under vacuum, at near normal incidence.

Results and Discussion

The goal of this investigation was to examine the potential of spinodal decomposition and nucleation and growth processes as a means to produce nanostructured bulk materials with enhanced phonon scattering over a wide range of temperatures. Because these are well-studied processes of phase segregation, if they could be proven to be important in promoting such scattering, it would have broad implications as to how to design bulk thermoelectrics with enhanced ZTs. We focused on the PbTe–PbS system because of its narrow-gap semiconductor character and its potential for high thermoelectric performance.[32] We first demonstrate the nanostructured biphasic nature of this system, using X-ray and transmission electron microscopy characterization. We then show nanostructuring results via a spinodal decomposition and nucleation and growth mechanism. Subsequently, we focus on electronic, optical, and transport properties of the material followed by thermal conductivity studies which point to a remarkable suppression of heat flow, coupled with a relatively facile electron flow through the structure. We demonstrate that a combination of these characteristics leads to a significant enhancement in the figure of merit ZT over that of the *non*-nanostructured PbTe, $Pb_{1-x}Sn_xTe$, and PbTe–PbSe systems at all temperatures.

Structural Characterization. Spinodal decomposition is an atomic level mechanism by which a metastable single phase (i.e., a solid solution) of two phases with volume fraction x can be made thermodynamically more stable by phase segregation. The necessary condition for the stability of a heterogeneous phase is that the chemical potential, G, of a component must increase with increasing x which means that $\partial^2 G/\partial x^2 > 0$, at a given temperature. If this condition is not met then the mixture is unstable (it will decompose) so that we can define a metastability limit, the so-called spinodal, where $\partial^2 G/\partial x^2 = 0$.[33] Spinodal fluctuations do not involve any crystalline transformation, since both components comprising the putative solid solution system are isomorphous. Instead they involve a spatial modulation of the local composition with wavelength, λ, in the range $2 \leq \lambda \leq 5$ nm. This spatial modulation can be exploited to create coherently embedded nanostructures of a given phase into a thermoelectric matrix and thus create nanostructured thermoelectrics on a large reaction scale. The spinodal decomposition phenomenon is well-known in various intermetallic[34] and polymer blend systems,[35,36] but less is known about it in semiconductors and insulators.[37–40]

Outside of the spinodal decomposition region phase separation occurs via the nucleation and growth mechanism. The latter requires large composition fluctuations to decrease the free energy.[41] For nucleation, in contrast to phase separation by spinodal decomposition, the nucleating phase must initiate with a composition that is *not* near that of the parent solid solution phase. Nucleation is a phase transition that is large in degree (composition change) but small in extent (size), whereas spinodal decomposition is small in degree but large in extent. Both lead to nanostructures, and both are relevant in the PbTe–PbS system.

The PbTe–PbS system was selected so that the nanostructuring idea could be explored based on the phase diagram which shows a well-defined spinodal curve.[17] The x values examined here were chosen so as to sample the various regions in the phase diagram. The published diagram indicates two separate regions, one where the spinodal decomposition regime dominates ($\sim 0.08 < x < \sim 0.90$) and the remainder where solid solution behavior dominates. The substitution of 5% mol of Sn to generate $(Pb_{0.95}Sn_{0.05}Te)_{1-x}(PbS)_x$ did not seem to cause any deviation from these properties. In this work we discovered that nucleation and growth also occurs especially when $x < 0.16$ although the exact limits of composition are not known. The $x = 0.16$ system is a compromise between having a substantial enough fraction of PbS to exhibit spinodal decomposition and at the same time the content being low enough to maintain a high carrier mobility for the system. Samples with 4%, 8%, and 30% PbS were also examined for further studies because the 4% concentration seemed to fall outside of the spinodal decomposition region, whereas the 30% samples were expected to be deep into it.

Figure 1 displays typical powder X-ray diffraction patterns for the $(Pb_{0.95}Sn_{0.05}Te)_{1-x}(PbS)_x$ with $x = 0.04$, 0.08, 0.16, and 0.30 samples. After peak indexing the existence of two phases,

(29) Thermophysical Properties Research Lab, 3080 Kent Ave. West Lafayette, IN 47906.
(30) Chung, D. Y.; Hogan, T.; Brazis, P.; Rocci-Lane, M.; Kannewurf, C.; Bastea, M.; Uher, C.; Kanatzidis, M. G. *Science* **2000**, *287* (5455), 1024–1027.
(31) Caillat, T.; Borshchevsky, A.; Fleurial, J. P. *J. Appl. Phys.* **1996**, *80* (8), 4442–4449.
(32) Gurieva, E. A.; Konstantinov, P. P.; Prokof'eva, L. V.; Pshenai-Severin, D. A.; Fedorov, M. I.; Ravich, Y. I. *Semiconductors* **2006**, *40* (7), 763–767.
(33) Cahn, J. W. *J. Chem. Phys.* **1965**, *42* (1), 93 ff.
(34) Cahn, J. W. *Acta Metall.* **1964**, *12* (12), 1457 ff.
(35) Pincus, P. *J. Chem. Phys.* **1981**, *75* (4), 1996–2000.
(36) Degennes, P. G. *J. Chem. Phys.* **1980**, *72* (9), 4756–4763.
(37) Jaw, D. H.; Chang, J. R.; Su, Y. K. *Appl. Phys. Lett.* **2003**, *82* (22), 3883–3885.
(38) Vavilova, L. S.; Kapitonov, V. A.; Murashova, A. V.; Pikhtin, N. A.; Tarasov, I. S.; Ipatova, I. P.; Shchukin, V. A.; Bert, N. A.; Sitnikova, A. A. *Semiconductors* **1999**, *33* (9), 1010–1012.
(39) Stringfellow, G. B. *J. Electron. Mater.* **1982**, *11* (5), 903–918.
(40) Shernyakov, Y. M.; Bedarev, D. A.; Kondrat'eva, E. Y.; Kop'ev, P. S.; Kovsh, A. R.; Maleev, N. A.; Maximov, M. V.; Mikhrin, S. S.; Tsatsul'nikov, A. F.; Ustinov, V. M.; Volovik, B. V.; Zhukov, A. E.; Alferov, Z. I.; Ledentsov, N. N.; Bimberg, D. *Electron. Lett.* **1999**, *35* (11), 898–900.
(41) Grovenor, C. R. M.; Hentzell, H. T. G.; Smith, D. A. *Acta Metall.* **1984**, *32* (5), 773–781.

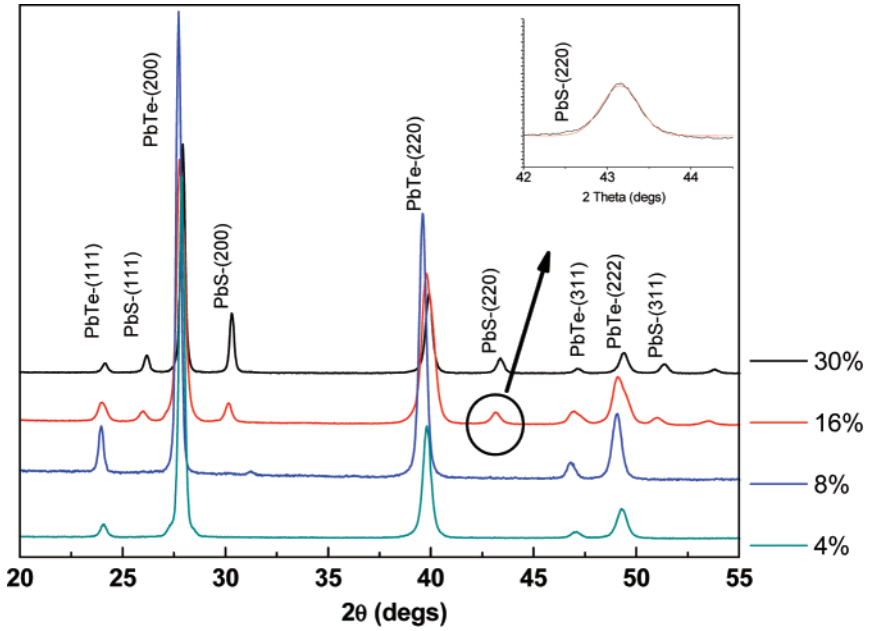

Figure 1. Typical powder X-ray diffraction of a $(Pb_{0.95}Sn_{0.05}Te)_{1-x}(PbS)_x$, $x = 0.16$ sample on which two phases, namely, PbTe and PbS, can be clearly identified and indexed. The inset shows a Gaussian fit to the PbS (220) peak which helped to define an average PbS particle size of 33 nm using the Scherrer analysis.

PbTe and PbS, was visible for the 16% and 30%.[42,43] The lower concentrations did not show a PbS signal due to the low detectivity of the experiment. For the 16% sample further analysis of the PbS (220) peak in the context of the Scherrer model (peak fitted to a Gaussian function) yielded an average PbS domain size of ~30−33 nm. Interestingly, the PbTe peaks were also found to be considerably broadened compared to those of the bulk micrometer-sized powder. This fact indicates shorter length scales for the two phases in the system than in the end-members.

Typical HRTEM images of $(Pb_{0.95}Sn_{0.05}Te)_{1-x}(PbS)_x$ with $x = 0.04$, 0.08, and 0.30 samples are shown in Figure 2, whereas those for the 16% sample are shown in Figure 3. The 4% samples showed a small degree of nucleation and growth phenomena with large regions being highly ordered suggesting solid solution behavior at this low concentration, Figure 2a. Nucleation and growth was more prevalent in the 8% samples, Figure 2b. The nanocrystals range in size from 3 to 10 nm. In addition, some local nanoscale compositional fluctuation due spinodal decomposition could readily be observed in the 8% samples, Figure 2, parts c and d, which became even more prevalent in the 16%, Figure 3, parts a and b, and became extensive in the 30% samples as the characteristic wavy pattern in Figure 2d. The 30% samples showed almost exclusively evidence for spinodal decomposition and no sign of nucleation and growth.

The HRTEM images of Figure 3 show that the 16% sample contains coexisting regions with spinodal decomposition and nucleation and growth phenomena. We observed regions of arbitrary shape that are 300−600 nm in length and 90−300 nm wide which in turn are made up of parallel stripes that have the

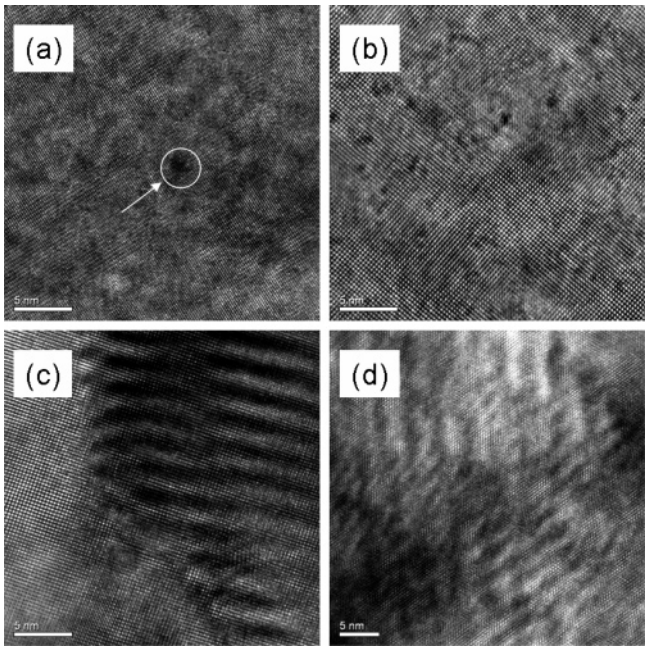

Figure 2. HRTEM images of the selected samples of (a) 4% showing mainly solid solution character with some nucleation and growth; (b) 8%, a region showing nucleation and growth; (c) 8%, a region showing spinodal decomposition; the parallel lines correspond to periodical compositional fluctuations of PbS (bright) and PbTe (dark) phases; both types of nanostructuring were observed in the 8% samples; (d) 30% showing predominantly spinodal decomposition. The scale bars are 5 nm.

width of the patch and are ~2 nm wide. These are characteristic spinodal decomposition. In addition, we also observe regions that contain particles ranging in size from 3 to 10 nm. The appearance of these nanoparticles is consistent with a nucleation and growth mechanism. Figure 3a−d shows a good example of a well-defined patch ~100 nm wide (~600 nm in length, not fully shown here) which partly consists of stripes (Figure 3a), stripes mixed with nanoparticles (Figure 3b), and nanoparticles (Figure 3, parts c and d). This region of the sample

(42) Here we do not imply pure phase separation. A certain solubility of one phase into the other is expected so that a more correct picture is a mixture of $PbTe_{1-x}S_x$ and $PbS_{1-x}Te_x$.

(43) The nanophase separation is supported by pair distribution analysis studies conducted on $(PbTe)_{1-x}(PbS)_x$: Lin, H; Bozin, E. S.; Billinge, S. J. L.; Androulakis, J.; Lin, C. H.; Kanatzidis, M. G. *Phys. Rev. B*, submitted for publication.

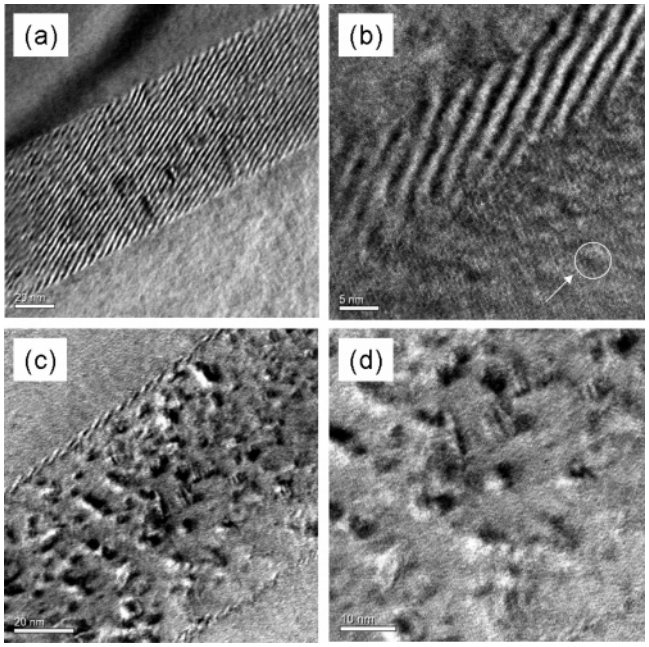

Figure 3. Characteristic HRTEM pictures of the investigated sample of PbS 16%. All pictures show parts of the same patch. (a) Spinodal decomposition of PbTe into PbS. The parallel lines correspond to periodical compositional fluctuations of PbS (bright) and PbTe (dark) phases. (b) Depending on the local S concentration, parts of the patch exit the spinodal region of the phase diagram and the characteristic compositional fluctuation fades away. (c and d) Outside the spinodal region the PbTe−PbS mixture is still unstable, but the two phases separate by nucleation and growth; thus, embedded nanoparticles of arbitrary shape appear.

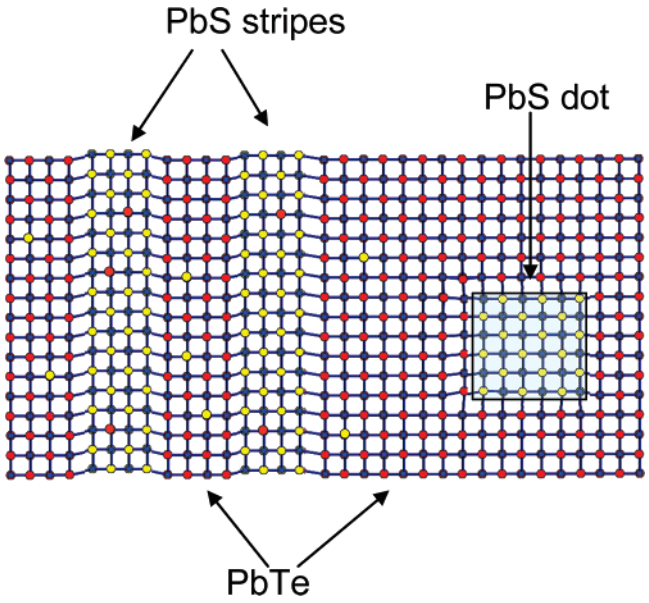

Figure 4. Structure of the $(PbTe)_{1-x}(PbS)_x$ system depicting the nanophase separation occurring via spinodal decomposition (stripes) and nucleation and growth (dot).

was further analyzed with the use of energy-dispersive spectroscopy (EDS), and the results are shown in Figure 5. Figure 5a depicts an area with a clearly discerned elongated narrow patch which is of the same type as that shown in greater magnification in Figure 3a. Figure 5b−d presents the elemental line maps for Pb La_1, Te La_1, and S Ka_1, respectively, that clearly show the patch to be S-rich and Te-poor. Therefore, we conclude that the narrow patch is made of PbS-rich phase which

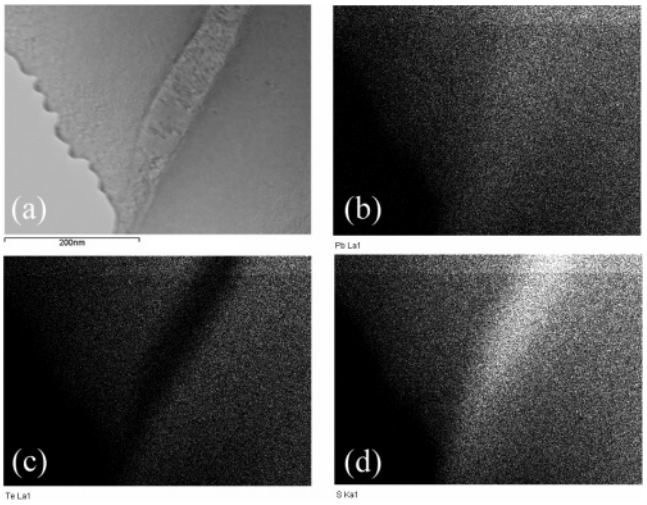

Figure 5. Energy-dispersive spectroscopy maps of a part of the HRTEM sample of PbS 16% showing a characteristic patch (a) details of which are depicted on Figure 3. Map b refers to the Pb La_1 line, map c to the Te La_1 line, and map d to the S Ka_1 line. The bright dots on each figure correspond to the individual element probed.

separates from the PbTe-rich matrix a result consistent with the X-ray diffraction.

Depending on the local composition, the phase segregation occurs either by a spinodal decomposition mechanism which occurs on the nanoscale and is of primary interest in this work and to certain extent by a nucleation and growth mechanism. Both mechanisms of nanostructuring offer the additional benefit of a high degree of coherence between the two phases potentially reducing charge scattering at the interfaces.[44] A schematic structure of the system highlighting the PbS-rich stripes created by spinodal decomposition and nanocrystals of PbS precipitated in a PbTe matrix is shown in Figure 4. In this series of samples, the degree of spinodal decomposition was higher with higher fraction of PbS in PbTe. The fraction of domains exhibiting nucleation and growth was higher in the 8% and 16% compositions. The 4% sample is the most dilute and tended to be closer to a solid solution; nevertheless, it too exhibited to a smaller degree nucleation and growth.

That the materials are macroscopically phase separated on the bulk scale comes from detailed studies of the average and local structures of the $(PbTe)_{1-x}(PbS)_x$ system using the Rietveld and atomic pair distribution function (PDF) methods.[43] Combining TEM data presented here and bulk X-ray scattering data suggests that these samples are a nanocomposite of PbTe-rich domains, containing nanoprecipitates created by a nucleation and growth mechanism and partially spinodally decomposed phase. This situation results in a nanometer scale inhomogeneous material that accounts for its very low thermal conductivity (vide infra). The phenomena described in this system are different in nature from the much larger layering features observed in the PbTe−Sb_2Te_3 system.[45]

(44) To make sure that the particles were not the result of debris byproducts from the ion-milling process, we carefully examined the area around the patch at high tilt angles. We found that a large concentration of particles exists only within the S-rich area. Furthermore, the existence of particles and lines is random in proximity to the perforated edge of the samples. Therefore, we conclude that ion-milling most probably has no effect on the structural features we observe within the patches.

(45) Ikeda, T.; Collins, L. A.; Ravi, V. A.; Gascoin, F. S.; Haile, S. M.; Snyder, G. J. *Chem. Mater.* **2007**, *19* (4), 763−767.

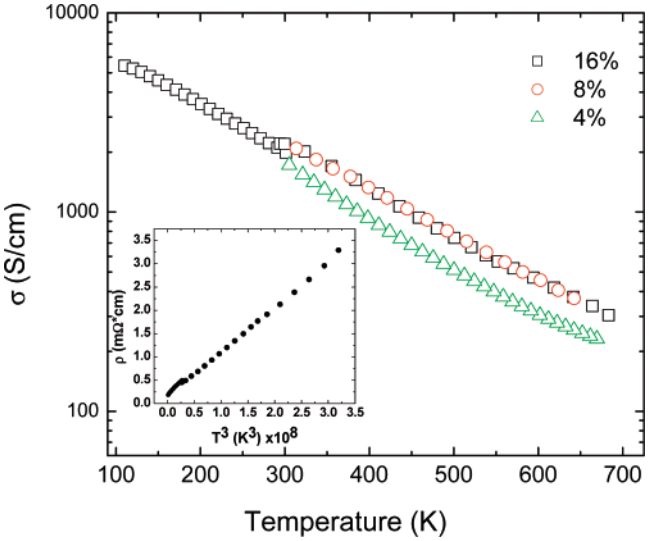

Figure 6. Electrical conductivity of $(Pb_{0.95}Sn_{0.05}Te)_{1-x}(PbS)_x$, $x = 0.04$, 0.08, and 0.16, as a function of temperature. The brake in the curve around 300 K occurred upon changing measurement apparatus from low to high temperatures. The inset depicts resistivity scaling of 16% with temperature as T^3.

Charge Transport. The of 4% and 8% samples both have high electrical conductivity with 1720 and 2090 S/cm at room temperature, decreasing to about 245 and 370 S/cm at 650 K as shown in Figure 6. The electrical conductivity values for the 16% sample were measured over a wide range of temperature between 100 and 700 K. At 100 K the conductivity was $\sim 6 \times 10^3$ S/cm, and it dropped to $\sim$300 S/cm at 700 K, see Figure 6. The electrical conductivity values for the 30% composition were very low at $\sim$30 S/cm from 300 to 675 K. The resistivity data for 4%, 8%, and 16% follow a $\rho = 1/\sigma \propto T^{\lambda}$, scaling law with $\lambda = 2.45$, 2.6, and 3, see the inset for 16% in Figure 6.

The retention of high conductivity values for the 4%, 8%, and 16% samples even at 700 K certainly points toward a high electronic mobility despite the macro- and nanoinhomogeneity of the system. This was confirmed by measurements of the Hall mobility for 16% in the temperature range of 100−700 K, see Figure 7. The Hall coefficient in this temperature range was negative indicative of n-type conduction. Assuming parabolic bands and single-band conduction processes in our analysis we determined the carrier concentration n to be $\sim 1.7-2 \times 10^{19}$ electrons/cm^3 ($n = 1/eR_H$, where e is the electronic charge and R_H is the Hall coefficient) and nearly constant with temperature. The Hall mobility, defined as $\mu_H = \sigma/ne$, at room temperature was 726 cm^2/V·s which lies almost midway between that of n-type PbS for $n \sim 2 \times 10^{19}$ cm^{-3} and n-type PbTe with $n \sim 9 \times 10^{18}$ cm^{-3}. Despite the large number of interfaces observed in the sample by HRTEM, μ_H remains above 100 cm^2/V·s at 700 K. Based on the observed relative insensitivity of the carrier concentration with temperature, we conclude that the electrical conductivity is mainly affected by factors influencing the mobility.

PbTe has a significantly larger mobility, $\sim 1-1.5 \times 10^3$ cm^2/V·s at 300 K for a carrier concentration of $\sim 5 \times 10^{18}$ cm^{-3}, compared to that of PbS, $\sim 5 \times 10^2$ cm^2/V·s at 300 K for 2×10^{19} cm^{-3}.[46] In the past low thermal conductivity has been

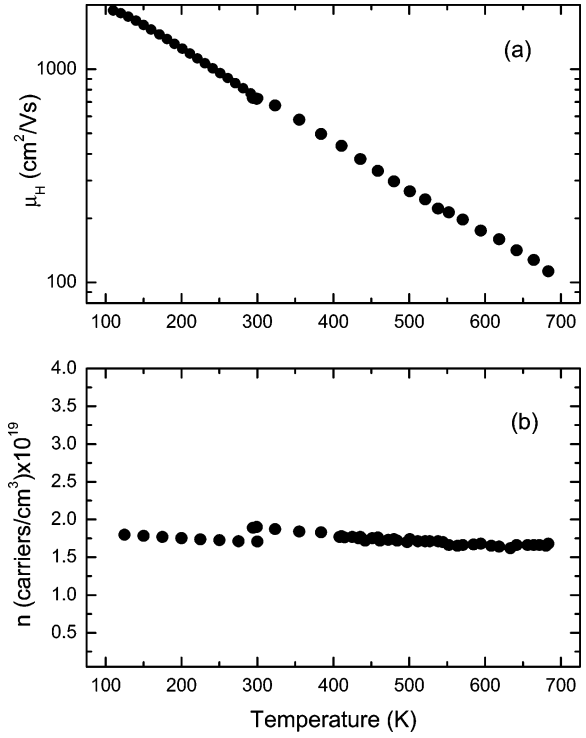

Figure 7. (a) Electron Hall mobility of $(Pb_{0.95}Sn_{0.05}Te)_{1-x}(PbS)_x$, $x = 0.16$, as a function of temperature. Notice the relatively high value (>100 cm^2/V·s) even at 700 K. (b) Carrier concentration as a function of temperature. The mismatch occurred upon changing apparatus from low to high temperatures.

reported for PbTe samples with PbS dilution as high as 10%.[47−49] However, the experimental details on the sample preparation were not provided and the studies were stated to have been performed on single-phase specimens, hence solid solutions. We show here that solid solutions are not stable in this system even at PbS concentrations as low as 4%.

In order to obtain an estimate of the carrier effective mass in the $(Pb_{0.95}Sn_{0.05}Te)_{1-x}(PbS)_x$ system, experimental reflectivity data were obtained from polished specimens of the 16% sample. The data were numerically analyzed using a classical oscillator superimposed by a Drude part that took into account the free carrier (plasmon) contribution. The experimental reflectivity spectrum and calculated curve are shown in Figure 8. The average effective mass of carriers m^*, was obtained from the relation,

$$\omega_p = \left(\frac{ne^2}{m^* e_\infty}\right)^{1/2}$$

where ω_p, n, and ϵ_∞ are the plasma frequency, carrier concentration, and the dielectric permittivity at high frequency, respectively. The value of n was determined from the Hall effect experiments, and ω_p and ϵ_∞ were extracted from fitting the reflectivity data. The analysis gave room-temperature effective mass m^* of $\sim 0.2m_e$, where m_e is the rest mass of the electron. This value roughly agrees with previous measurements on n-type

(46) Allgaier, R. S.; Scanlon, W. W. *Phys. Rev.* **1958**, *111* (4), 1029−1037.
(47) Kakhramanov, K. S.; Aliev, S. A. *Inorg. Mater.* **1982**, *18* (10), 1460−1464.
(48) Alekseeva, G. T.; Efimova, B. A.; Logachev, Y. A. *Sov. Phys. Semicond.* **1975**, *9* (1), 83−84.
(49) Alekseev, G. T.; Efimova, B. A.; Ostrovsk, L. M.; Serebrya, O. S.; Tsypin, M. I. *Sov. Phys. Semicond.* **1971**, *4* (7), 1122 ff.

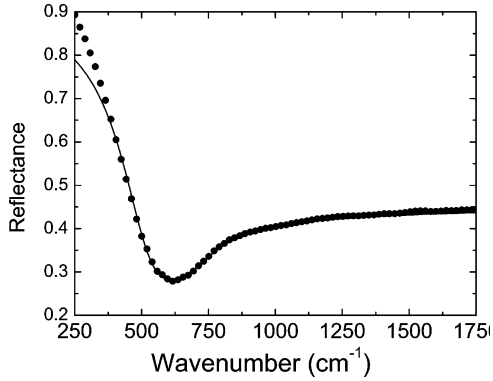

Figure 8. Typical room-temperature experimental (dots) and calculated (continuous line) reflectivity spectrum of PbTe−PbS 16%.

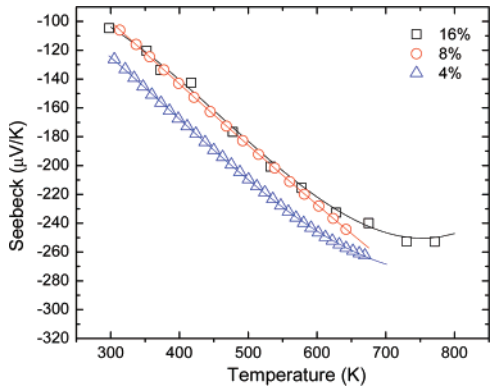

Figure 9. Seebeck coefficient of $x = 0.04$, 0.08, and 0.16 samples as a function of temperature measured in the range of $300 \leq T \leq 800$ K. The solid lines serve as a guide to the eye. The thermoelectric power response exhibits a peak around 750 K.

crystals of PbTe that showed $\sim 0.1 m_e$.[50] Therefore, it would appear that the introduction of nanoscale features in the PbTe matrix through the spinodal decomposition or nucleation and growth mechanism does not affect extensively carrier scattering across the relatively large number of dissimilar but mainly coherent interfaces.

Figure 9 presents the Seebeck coefficient of the $x = 0.04$, 0.08, and 0.16 samples as a function of temperature. The thermoelectric power response is negative in agreement with the Hall effect results for an n-type semiconductor obtained by doping with 0.055mol% PbI_2. The highest room-temperature thermopower value we measured was ~ -120 μV/K for the 4% sample which increased almost linearly to -260 μV/K at $\sim$670 K. At temperatures higher than 700 K the thermopower tends to reach a maximum absolute value and then decreases, indicative of cross-gap excitations generating holes (onset of intrinsic conduction). The optimum properties were observed for the 8% sample of this study resulting in a high-temperature power factor of ~ 22 μW/cm·K^2 at 642 K. For the 30% sample, although the thermopower at room temperature was ~ -320 μV/K, further high-temperature measurements were not pursued because of the very low electrical conductivity of this sample.

Thermal Conductivity. The most extraordinary aspect of the $(Pb_{0.95}Sn_{0.05}Te)_{1-x}(PbS)_x$ materials is the very low lattice thermal conductivity that they exhibit. The thermal conductivity is lower than what would be expected from simple solid solutions. Figure 10 shows the total thermal conductivity of the PbTe−PbS system for 4%, 8%, 16%, and 30%.

The electronic contribution to κ was calculated using the Wiedemann−Franz (WF) law assuming the Lorenz number to be 2.44×10^{-8} W Ω K^{-2} (for degenerate semiconductors). The derived lattice thermal conductivity at room temperature is only 0.84, 0.38, 0.40, and 1.01 W/m·K for 4%, 8%, 16%, and 30%, respectively.[51,52] It is indeed exceptional for bulk thermoelectric materials with a high mobility to exhibit such low lattice thermal conductivity. Interestingly, the lowest values are not observed for the 30% sample but for the 8% and 16% samples. The values for the latter sample are directly comparable to an estimate made by Harman on thermoelectric thin film superlattices of PbTe/PbSe which yielded 0.33 W/m·K, and the value is certainly much lower than the data reported for the parent compounds and some of their mixtures, see Table 1. This suggests that nanostructures exhibiting nucleation and growth may be more effective in scattering phonons than those created by spinodal decomposition. In addition, the effect of Sn substitution in the lattice is not believed to play a significant role in affecting the thermal conductivity since the difference between the lattice thermal conductivity of PbTe and $Pb_{0.95}Sn_{0.5}Te$ is negligible.[53]

The reasons for why nucleation and growth may be more effective in scattering phonons are not clear; however, it would appear that the interface area between the two phases may be larger in the former than in the latter. Moreover, the larger compositional contrast created by the nucleation and growth process vis-à-vis spinodal decomposition could be giving rise to a larger acoustic mismatch[54−56] between the two different phases, which can help to enhance the acoustic phonon scattering.

Another important observation is that the temperature dependence of κ_{lat} does not follow the usual Debye−Peierls prediction of $\sim 1/T$. Assuming an ionic crystal and a typical sound velocity of $\sim 5 \times 10^5$ cm/s[57] we calculate a phonon mean free path of $\ell \sim 2$ Å, which is considerably smaller than the unit cell size of $\sim$6.5 Å. Hence, the typical mechanism of collective phonon−phonon interactions giving rise to $1/T$ dependence of κ_{lat} does not apply in this case, and other mechanisms prevail.

The small rise of κ_{lat} from 0.4 W/m·K at 300 K to $\sim$0.6 W/m·K at 700 K for $x = 0.16$ may be due to a number of physical reasons such as (a) the scattering parameters are changing with temperature which would make the Lorenz number different from the classical value used in the calculation, (b) anharmonic phonon excitation that may play a role in increasing κ_{lat} at high

(50) Lyden, H. A. *Phys. Rev. A: Gen. Phys.* **1964**, *135* (2A), A514 ff.

(51) Kumar, G. S.; Prasad, G.; Pohl, R. O. *J. Mater. Sci.* **1993**, *28* (16), 4261−4272.

(52) The magnitude of the lattice thermal conductivity depends on the value of the Lorenz number used. We use here its absolute maximal value applicable for a degenerate metal or degenerate semiconductor and at temperatures >300 K (ref 50). The doping levels of the title materials at $\sim 2 \times 10^{19}$ cm^{-3} are close to the degenerate regime. The value could be lower for a nondegenerate semiconductor, and if so, the lattice thermal conductivities would be $\sim$20−30% higher.

(53) Orihashi, M.; Noda, Y.; Chen, L.; Hirai, T. *J. Jpn. Inst. Met.* **1999**, *63* (11), 1423−1428.

(54) Swartz, E. T.; Pohl, R. O. *Rev. Mod. Phys.* **1989**, *61* (3), 605−668.

(55) Swartz, E. T.; Pohl, R. O. *Appl. Phys. Lett.* **1987**, *51* (26), 2200−2202.

(56) Huxtable, S. T.; Abramson, A. R.; Tien, C. L.; Majumdar, A.; LaBounty, C.; Fan, X.; Zeng, G. H.; Bowers, J. E.; Shakouri, A.; Croke, E. T. *Appl. Phys. Lett.* **2002**, *80* (10), 1737−1739.

(57) Kittel, C. *Introduction to Solid State Physics*, 7th ed.; John Wiley and Sons: 2004.

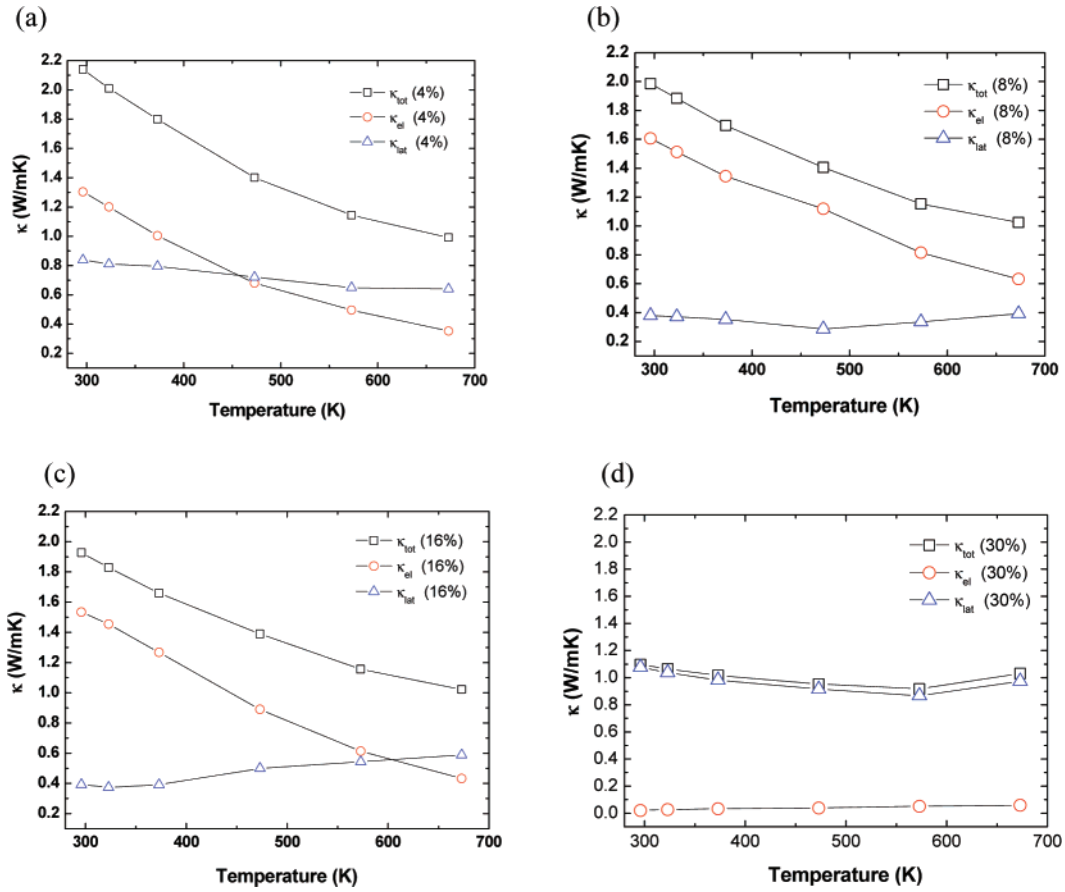

Figure 10. Thermal conductivity (open squares) of $(Pb_{0.95}Sn_{0.05}Te)_{1-x}(PbS)_x$, $x = 0.04$, 0.08, 0.16, and 0.30, determined by the flash diffusivity–heat capacity method. Extraction of the electronic (circles) and lattice (triangles) parts was done on the basis of the Wiedemann–Franz law. A fit of the electrical conductivity data has been used in order to get values at corresponding temperatures where the thermal diffusivity and the heat capacity of the sample were measured.

Table 1. Comparison of the Room-Temperature Lattice Thermal Conductivity of the Spinodally Decomposed PbTe–PbS System with Bulk PbTe and PbS, Two of Their Solid Solutions, and PbTe/PbSe Superlattices

compound	κ_{lat} (W/m·K)
PbTe, bulk	2.10[a]
PbS, bulk	2.50[b]
$Pb_{0.95}Sn_{0.05}Te$	2.10[c]
$PbTe_{0.95}S_{0.05}$, solid solution	1.21[a]
$PbTe_{0.9}S_{0.1}$, solid solution	1.01[a]
$(Pb_{0.95}Sn_{0.05}Te)_{1-x}(PbS)_x$, $x = 0.04$ (solid solution with some nucleation and growth)	*0.84*
$(Pb_{0.95}Sn_{0.05}Te)_{1-x}(PbS)_x$, $x = 0.08$ (nucleation and growth with some spinodal decomposition)	*0.38*
$(Pb_{0.95}Sn_{0.05}Te)_{1-x}(PbS)_x$, $x = 0.16$ (nucleation and growth and spinodal decomposition)	*0.40*
$(Pb_{0.95}Sn_{0.05}Te)_{1-x}(PbS)_x$, $x = 0.30$ (spinodal decomposition)	*1.08*
PbTe/PbSe, superlattice	0.33[d]

[a] Ref 28. [b] Ref 32. [c] Ref 53. [d] Ref 8.

temperatures, or (c) partial local collapse of the nanostructures at high temperatures. These possibilities will be tested in future studies. Previous studies on similar PbTe/PbSe/PbS systems assumed a solid solution behavior, and the low thermal conductivity values observed were attributed to the S atoms occupying off-center positions in the solid solution.[32,58] The work presented here suggests that nanophase separation is likely a more relevant mechanism responsible for the very low thermal conductivity and not a solid solution nature of the system. In addition, pair distribution studies performed on the PbTe–PbS systems (8%, 16%, and 30%) confirm the nanophase separation and show no evidence of off-centering for any of the atoms involved.[43]

The apparent very low thermal conductivity of these nanostructured materials has a direct impact on the thermoelectric figure of merit. Samples of $(Pb_{0.95}Sn_{0.05}Te)_{1-x}(PbS)_x$ at $x = 0.16$ exhibited ZT values of up to ~1.28 at 660 K, whereas at $x = 0.08$ even higher ZT values of up to ~1.50 at 642 K were obtained. Samples with 4% of PbS have their highest ZT value of 1.10 at 642 K, Figure 11.

The current work supports the hypothesis that nanostructures can lead to marked improvements of thermoelectric properties in bulk systems. The present investigation now also provides a reasonable explanation for the significantly lower thermal conductivity of the PbTe–PbS samples compared to those of the corresponding $PbTe_{1-x}Se_x$ solid solution alloys.[59] With a minuscule thermal conductivity established, the current system presents an exciting materials platform with which to pursue high figure of merit through further refinement and control of the spinodal decomposition vis-à-vis nucleation and growth process and of course carrier doping.

(58) Gurieva, E. A.; Konstantinov, P. P.; Prokof'eva, L. V.; Ravich, Y. I.; Fedorov, M. I. *Semiconductors* **2003**, *37* (3), 276–282.
(59) Devyatko, E. D.; Tikhonov, V. V. *Sov. Phys. Solid State* **1965**, *7* (6), 1427 ff.

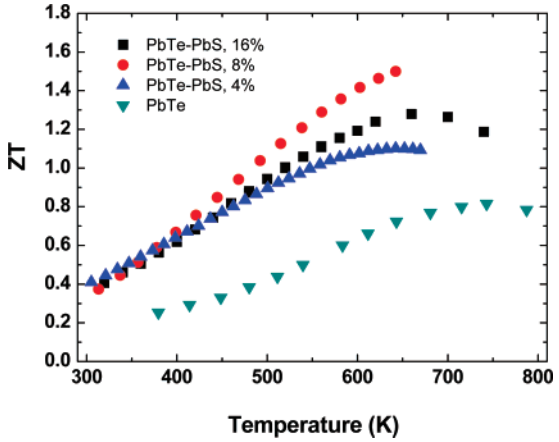

Figure 11. Dimensionless figure of merit as a function of temperature which peaks at ZT of 1.28 at 660 K for $x = 0.016$, 1.50 at 642 K for $x = 0.08$, and 1.10 at 642 K for $x = 0.04$.

Depending on the PbTe/PbS ratio the system exhibits nanostructuring via both nucleation and growth phenomena and spinodal decomposition. The latter mechanism predominates at high PbS fractions, whereas the former seems to prevail at lower fractions. The reasons for the inability of the PbTe/PbS system to form solid solutions (except perhaps at very low concentrations of PbS, e.g., <3%) could lie in the very different lattice parameters between the sulfide and telluride compounds which leads to large lattice mismatch and strain.

Concluding Remarks

The system $(PbTe)_{1-x}–(PbS)_x$ is in fact nanostructured and not a solid solution over a wide range of concentrations. It exhibits spinodal decomposition and or nucleation and growth depending on x. This nanophase segregation is characterized by fluctuations in local sulfur concentration giving rise to high density of nanostructural features at three length scales. We have shown that this nanocomposite system substantially retains the high electron mobility of PbTe and combines it with a remarkably low lattice thermal conductivity of ~0.40 W/m·K, especially when the PbS fraction is in the range of 8−16%. These findings are in agreement with recent theories and experiments that point toward a very low thermal conductivity in semiconducting nanostructures. Interestingly, compositions in which nucleation and growth was the predominant mode of nanostructuring had lower lattice thermal conductivities that those dominated by spinodal decomposition. We can therefore qualitatively assess the relative importance of the two observed modes of nanostructuring in suppressing the thermal conductivity and can conclude that nucleation and growth seems more effective.

A combination of high carrier mobility and low lattice thermal conductivity is the foundation for realizing an enhanced figure of merit. The PbTe−PbS system indeed appears to be a very promising thermoelectric material for power generation application in the temperature range of 500−700 K.

To the best of our knowledge, spinodal decomposition and nucleation and growth have not been considered as mechanisms for the intentional creation of nanostructuring thermoelectrics. Therefore, other related systems which also exhibit spinodal decomposition or nucleation and growth phenomena, such as the PbTe−EuTe system, are prime candidates for investigation.[60,61] The results presented here point to the need for detailed studies in these systems and especially the exploration of the influence of the nanostructure on the lattice thermal conductivity and ultimately the figure of merit.

Acknowledgment. The authors thank Professor S. D. Mahanti for useful discussions. The 200 kV field emission gun transmission electron microscope was acquired with an NSF Grant (DMR-0079578) (MSU Center for Advanced Microscopy). Financial support from the Office of Naval Research is gratefully acknowledged (N00014-03-10789 MURI program and N00014-06-10130). Part of this work was performed at the Jet Propulsion Laboratory/California Institute of Technology, under contract with NASA. K.M.P. acknowledges the financial support of Greek Secretariat of Research under the bilateral project with Non-European countries.

JA071875H

(60) Salamancayoung, L.; Partin, D. L.; Heremans, J. *J. Appl. Phys.* **1988**, *63* (5), 1504−1508.
(61) Salamancayoung, L.; Nahm, S.; Wuttig, M.; Partin, D. L.; Heremans, J. *Phys. Rev. B* **1989**, *39* (15), 10995−11000.